The Astrophysical Journal, 771:104 (13pp), 2013 July 10 doi:10.1088/0004-637X/771/2/104

FLARE RIBBON ENERGETICS IN THE EARLY PHASE OF AN *SDO* FLARE

L. Fletcher[1], I. G. Hannah[1], H. S. Hudson[1,3], and D. E. Innes[2]
[1] School of Physics and Astronomy, SUPA, University of Glasgow, Glasgow, G12 8QQ, UK
[2] Max Planck Institute for Solar System Research, Max-Planck-Strasse 2, D-37191 Katlenburg-Lindau, Germany
Received 2012 June 22; accepted 2013 May 16; published 2013 June 21

ABSTRACT

The sites of chromospheric excitation during solar flares are marked by extended extreme ultraviolet ribbons and hard X-ray (HXR) footpoints. The standard interpretation is that these are the result of heating and bremsstrahlung emission from non-thermal electrons precipitating from the corona. We examine this picture using multi-wavelength observations of the early phase of an M-class flare SOL2010-08-07T18:24. We aim to determine the properties of the heated plasma in the flare ribbons, and to understand the partition of the power input into radiative and conductive losses. Using *GOES*, *SDO*/EVE, *SDO*/AIA, and *RHESSI*, we measure the temperature, emission measure (EM), and differential emission measure of the flare ribbons, and deduce approximate density values. The non-thermal EM, and the collisional thick target energy input to the ribbons are obtained from *RHESSI* using standard methods. We deduce the existence of a substantial amount of plasma at 10 MK in the flare ribbons, during the pre-impulsive and early-impulsive phase of the flare. The average column EM of this hot component is a few times 10^{28} cm^{-5}, and we can calculate that its predicted conductive losses dominate its measured radiative losses. If the power input to the hot ribbon plasma is due to collisional energy deposition by an electron beam from the corona then a low-energy cutoff of ∼5 keV is necessary to balance the conductive losses, implying a very large electron energy content. Independent of the standard collisional thick-target electron beam interpretation, the observed non-thermal X-rays can be provided if one electron in 10^3–10^4 in the 10 MK (1 keV) ribbon plasma has an energy above 10 keV. We speculate that this could arise if a non-thermal tail is generated in the ribbon plasma which is being heated by other means, for example, by waves or turbulence.

Key words: Sun: activity – Sun: chromosphere – Sun: flares – Sun: UV radiation – Sun: X-rays, gamma rays

Online-only material: color figures

1. INTRODUCTION

How does the solar chromosphere in a flare evolve from its quiescent, pre-flare state to being the source of intense radiation and the site of energy deposition by non-thermal particles during the flare impulsive phase? Many multi-wavelength observations of the impulsive phase illuminate both thermal and non-thermal properties of the lower atmosphere, but detailed observations of the early stages of a solar flare—clearly a crucial part of the overall event—are sparse. In this paper, we aim to characterize the flare's initial heating and brightenings, and the ramp-up of particle acceleration. We present multi-instrument observations of SOL2010-08-07T18:24, an M-class event in which the early evolution of flare ribbons and loops can be followed in detail, and the temperature, emission measure (EM), electron and plasma energy content, and luminosity of the flare ribbons can be inferred.

Pre-flare studies are rather rare, in part due to flare triggers on previous missions which tended to start high-cadence observations only once the flare region became comparatively bright. Work has also tended to concentrate on the temporal and spatial relationships between pre-flare and flare sources, rather than on the physical conditions in the early phase. For example, Fárník et al. (1996) and Fárník & Savy (1998) could find no clear spatial relationship between pre-flare and flare sources observed with the *Yohkoh* soft X-ray telescope, and using the *Transition Region and Coronal Explorer* and *Yohkoh*/HXT, Warren & Warshall (2001) found that the first HXR bursts of a flare tend to occur in ultraviolet footpoints that show no activity before the flare HXRs start. A recent study of the early emission from a *GOES* B4.8 flare with the Atmospheric Imaging Assembly (AIA) on the *Solar Dynamics Observatory* (*SDO*) and the Coronal Diagnostic Spectrometer on the *Solar and Heliospheric Observatory* showed that in microflares chromospheric emission precedes hot plasma emission by about 6 minutes (Brosius & Holman 2012). The spatial correspondence of pre-flare source locations and other activity signatures has also been investigated—for example, Chifor et al. (2006, 2007) examined soft X-ray (SXR), hard X-ray (HXR), and extreme ultraviolet (EUV) pre-flare brightenings in events exhibiting filament ejection, finding evidence for heating and electron acceleration up to 50 minutes before a flare which was interpreted as evidence for pre-flare reconnection leading to filament destabilization and eruption.

In this paper, we use a combination of data from the *Ramaty High Energy Solar Spectroscopic Imager* (*RHESSI*; Lin et al. 2002), *SDO* Extreme UV Variability Experiment (EVE; Woods et al. 2012), and AIA (Lemen et al. 2012), supported by *GOES* X-ray measurements, to quantify the thermal and non-thermal energy content and luminosity in early flare ribbons. The consistent data set afforded by these instruments allows us to investigate the physical properties of the flare plasma during the first 10–15 minutes of its development.

2. OVERVIEW OF THE EVENT

We will be concerned with the physical properties of the flare ribbons during the first 10–15 minutes of the flare, rather than its evolution overall, but the event is interesting and merits a brief description. SOL2010-08-07T18:24 was an M1.0 class flare occurring in NOAA active region 11093—the only major

[3] Space Sciences Laboratory, University of California Berkeley, 7 Gauss Way, Berkeley, CA 94720, USA.

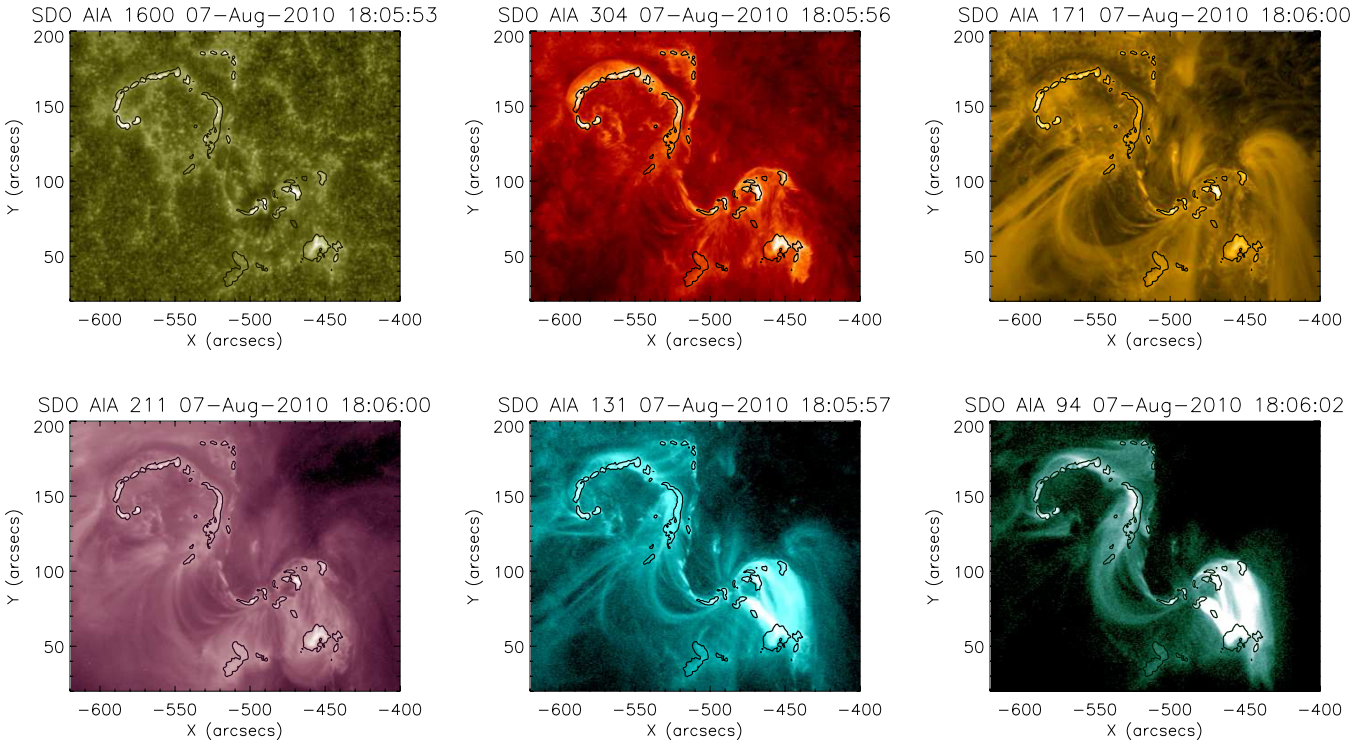

Figure 1. Almost simultaneous images of the flaring region in various *SDO*/AIA filters. 211 Å channel contours at 700 DN s^{-1} $pixel^{-1}$ are overplotted on all panels. Images have been logarithmically scaled.

(A color version of this figure is available in the online journal.)

event reported from this region. The active region was the only one present on the solar disk at that time. It had one strong negative polarity sunspot in the southeast, and dispersed positive plage in the northwest. The plage hosted an inverse-S shaped filament, the southern part of which was apparently rooted in the sunspot. The flare was associated with the lifting-off of the upper portion of the filament, which began a slow rise at 17:40 UT, as studied in detail by Vemareddy et al. (2012) and by Liu et al. (2012). Prior to the flare, a set of loops rooted in the southern sunspot was very bright in EUV and X-rays (see Sections 4.2 and 5), and dots of EUV emission were visible in the sunspot umbra and penumbra from 17:52 UT onward. The flare ribbons started to become visible around 17:54 UT and appeared initially as elongated EUV brightenings along the northern part of the filament that remained along the polarity inversion line. These early ribbon brightenings were very close to, or perhaps even within, the dark filament material. The filament is clearly visible in the 304 Å, 171 Å, and 211 Å images in Figure 1, which shows logarithmically scaled *SDO*/AIA images, taken about half way through the rise phase. The northern flare ribbons are visible in all wavelengths, and the southern loops are present in the higher temperature filters, particularly the 94 Å images.

As the upper portion of the filament accelerated away, the flare ribbons intensified and spread rapidly outward from the remaining filament material. We note in passing that the partial ejection of the filament is consistent with reconnection internal to the filament, or between its upper and lower parts (e.g., Tripathi et al. 2009). Dynamics in the decay phase of the event are reported in Srivastava & Murawski (2012).

3. *GOES* DATA

The *GOES* light curve is shown in Figure 2, along with the EM and temperature calculated with the *GOES* graphical user interface in the IDL SolarSoft library, having first subtracted the pre-flare background. This flare occurred in an otherwise completely quiet period so the background level is well-defined, and was taken between 16:00 UT and 17:00 UT. Data in the 0.5–4 Å channel are noisy before around 17:55 UT, so the derived temperature and EM values are unreliable during this time. A rapid rise and bump in the *GOES* data between 17:56 UT and 18:05 UT is accompanied by a slow rise in the EM to a value of 6×10^{47} cm^{-3}, and an increase of the *GOES* temperature to 10 MK. Thereafter the EM rises rapidly to a peak of 7×10^{48} cm^{-3}, at 18:25 UT. As we will show in Section 4.3 the first increase in EM and temperature is associated with the southern loops, and after ∼18:06 UT the flare ribbons start to dominate.

4. *SDO* DATA OVERVIEW AND ANALYSIS

4.1. *SDO*/EVE Spectra and Light Curves

The MEGS-A spectrometer, one component of the EVE instrument (Woods et al. 2012), covers the wavelength range 64–370 Å, at a resolution of about 1 Å, with 0.2 Å binning in wavelength and 10 s binning in time (Crotser et al. 2007; Hock et al. 2012). The instrument sees the whole Sun, and the flare emission is a small perturbation on a strong background. However, the spectra are very stable so the pre-flare spectrum can be subtracted to leave the flare enhancement. We will use the *SDO*/EVE to estimate contributions to the total flare luminosity, and as a quick way to examine the time evolution of the flare in each of the AIA passbands used for imaging.

The response in *SDO*/AIA can be simulated by convolving the EVE spectrum with the *SDO* spectral response (Boerner et al. 2012). This is possible for all of the AIA EUV filters, and also the 304 Å filter. The *SDO*/AIA EUV filters are narrow

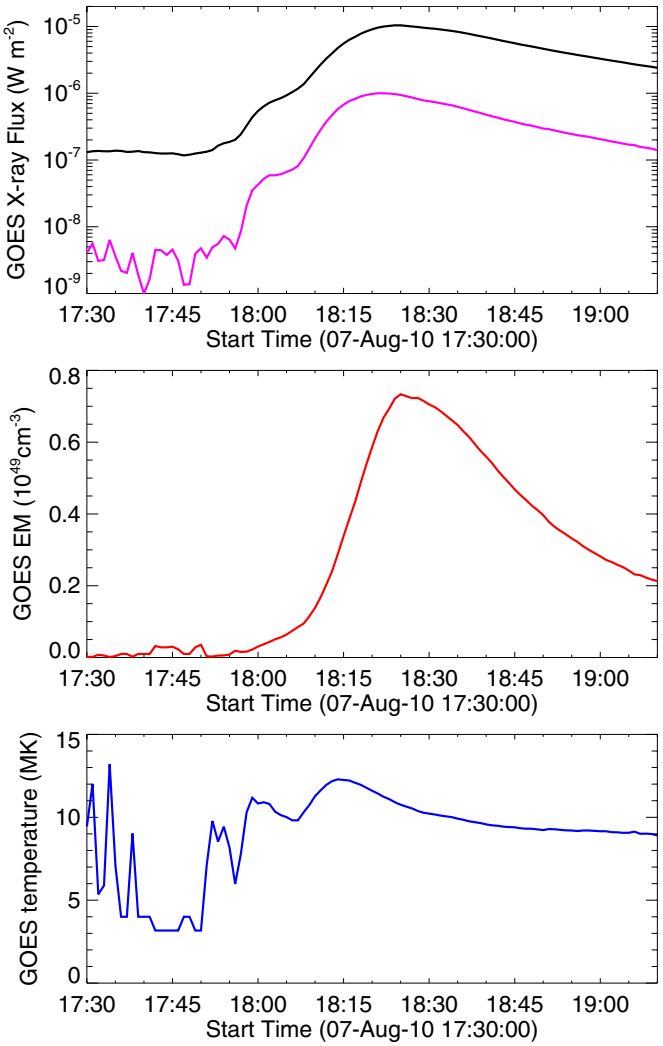

Figure 2. *GOES* X-ray flux (upper), emission measure (middle), and temperature (lower). In the upper panel the black line is the 1–8 Å flux, and the pink line is the 0.4–4 Å flux.

(A color version of this figure is available in the online journal.)

and centered on certain strong emission lines of iron, but these lines are superposed on a time-varying continuum (Milligan et al. 2012), which can also be strong, particularly in very hot events (see, e.g., Feldman et al. 1999; Warren & Reeves 2001). Figure 3 (left panel) shows light curves obtained by convolving the observed EVE spectrum with the AIA filter responses. The synthesized 304 Å light curve rises earliest of all the emissions plotted, as would be expected from modest excitation of the lower atmosphere. This corresponds to brightening of the chromospheric ribbons.

During the flare rise phase, the (normalized) synthesized 131 Å channel light curve tracks the (normalized) *GOES* 1–8 Å flux best of all the AIA passbands, suggesting a significant high temperature plasma contribution in the 131 Å channel. O'Dwyer et al. (2010) calculated contributions to the AIA EUV passbands using a prescribed flare differential emission measure (DEM), albeit one representing the decay phase of an M2 flare (Dere & Cook 1979), and showed that the 131 Å channel is expected to be dominated by Fe XXI at 128.75 Å formed at a temperature of 11 MK. However, there is also a low temperature contribution in this passband, dominated by the Fe VIII pair at 130.94 Å and 131.24 Å formed at 400,000 K (see also Brosius & Holman 2012). These are not expected to be strong, but we check this by using EVE to measure the flaring excess integrated over the Fe VIII and Fe XXI lines. This is plotted in the right hand panel of Figure 3, which compares the absolute irradiance in *GOES* 1–8 Å and the excess irradiance in the Fe XXI line (red) and the Fe VIII pair (blue). Note, at the wavelength position of the Fe VIII pair there is no spectral feature apparent; the counts are consistent with the background level. So the blue points plotted are mostly indicating the background continuum intensity, and should be considered only as upper limits to the Fe VIII line intensity. The excess is calculated with respect to a 5 minute quiet-Sun average irradiance taken before the flare starts. It is clear from its intensity and its evolution that the hot Fe XXI-emitting plasma is the main contributor to the AIA/131 Å channel throughout the flare. This is consistent with the temperatures derived from the *GOES* channel ratio in Figure 2.

We note also that the intensities in the other spectral passbands peak well after the *GOES* peak, consistent with a plasma cooling from high to low temperatures. The moderate-temperature channels (171 Å, 193 Å, and 211 Å) show intensity decreases after 18:15 UT, which may be consistent with a low-temperature coronal dimming. However, as the focus of this paper is on the flare rise phase we will not consider the late-phase development any further.

4.2. SDO/AIA Imaging

We use AIA level 1 data, converted to level 1.5 data using the SolarSoftWare `aia_prep` routine, and normalized by the

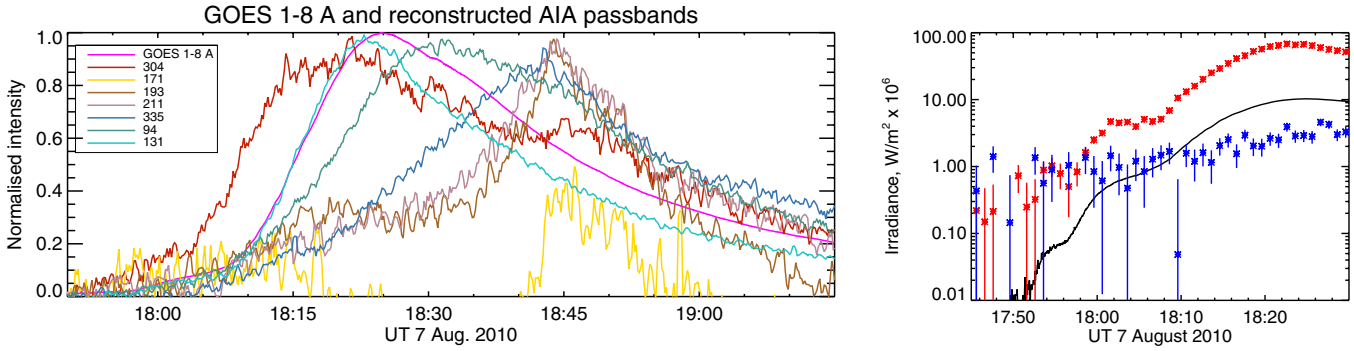

Figure 3. Left: normalized light curves of *GOES* 1–8 Å and synthesized AIA intensities from EVE spectra. The synthesized AIA intensities have been smoothed with a three-point boxcar. Right: the *GOES* 1–8 Å light curve and the flare excesses in the two primary lines featuring in the AIA/131 Å channel, i.e., Fe XXI at 128.75 Å (red) and the Fe VIII pair at 130.94 Å and 131.24 Å (blue, intensity upper limits).

(A color version of this figure is available in the online journal.)

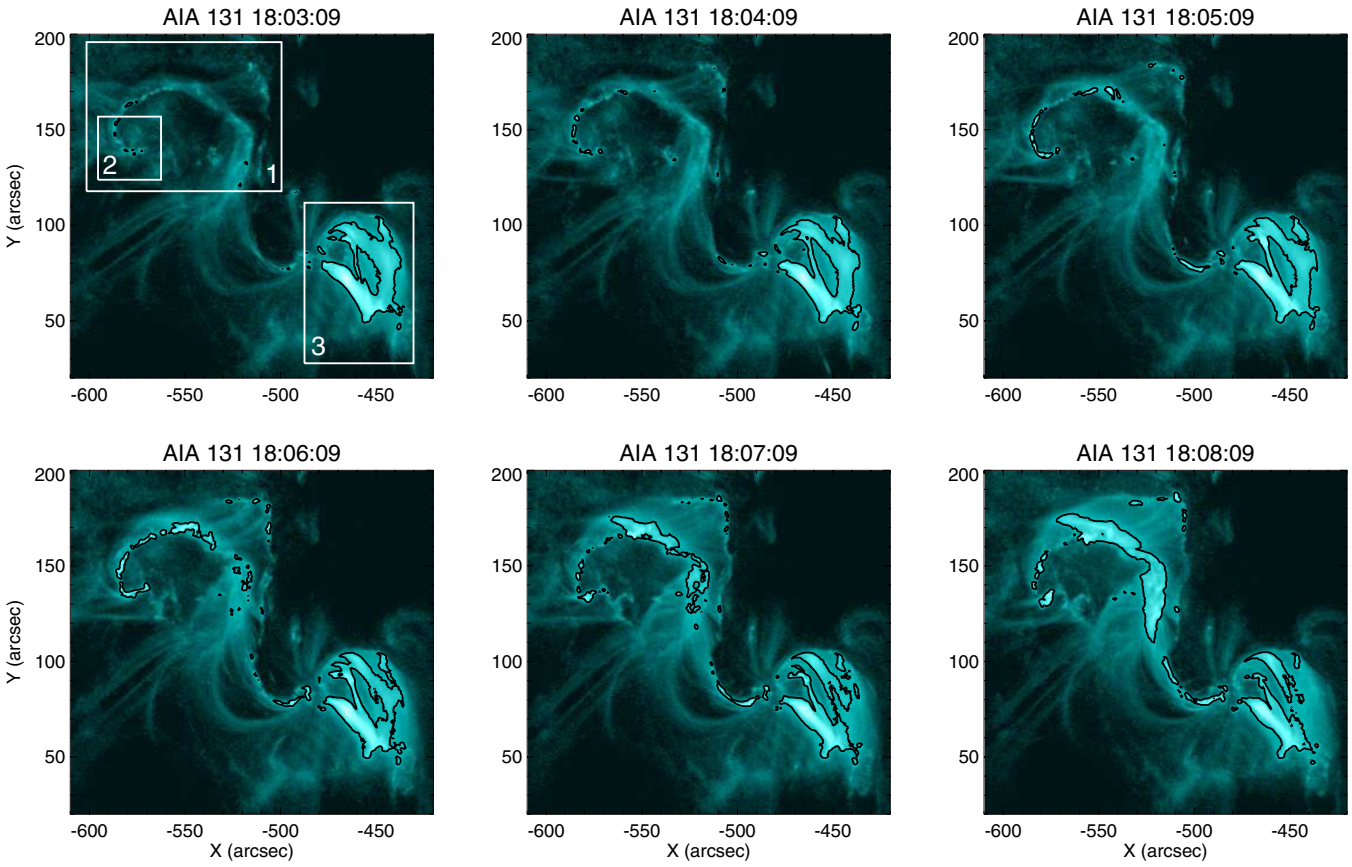

Figure 4. *SDO*/AIA 131 Å channel images, with contours drawn at 175 DN s^{-1} $pixel^{-1}$. Summing inside these contours results in the light curves in Figure 5. Boxes in the top left image outline three different regions of interest: (1) northern ribbons, (2) subset of these ribbons, referred to as the northern footpoints, and (3) southern loops. The image intensity has been logarithmically scaled.

(A color version of this figure is available in the online journal.)

exposure time. The data have been despiked, and inspection of the despiked pixel locations shows that only around 10 flaring pixels per image have been removed over the time of interest. The main flare ribbons in the north start to appear around 17:54 UT, and are well-defined, mostly unsaturated, and easy to distinguish from the main loop arcade that starts to brighten from around 18:10 UT onward. The location of ribbons is compared across AIA channels in Figure 1. Contours at 700 DN s^{-1} $pixel^{-1}$ from the 211 Å filter are overlaid on the other images. There is a very good correspondence—at the level of one or two pixels—between the brightest ribbon sources in the north across the AIA wavelength range. Several other sources in the southern sunspot area are also spatially well-correlated. This indicates that the ribbons emit across a broad range of temperatures, from around 100,000 K to ~10 MK.

4.3. AIA 131 Å and GOES Light Curves

The two main parts of the flare—the northern ribbons and the southern loops—have quite different characteristics, and the overall light curve in the AIA passbands is a composite of these. In Section 4.1 we demonstrated that the synthesized 131 Å light curve most closely matches the *GOES* light curves, and with *SDO*/AIA imaging the 131 Å light curve can be decomposed into contributions from the different regions shown in Figure 4. We separate the flare into three regions: the bright loops near the sunspot, at around $(-470'', 70'')$, the ribbons and loops to the northeast of these, and then a subset of pixels in the ribbons (referred to as the "northern footpoints") which are not so affected by the presence of loops later in the event. These regions are shown in Figure 4. We sum emission from sources within each of these three boxes having intensity above 175 DN s^{-1} $pixel^{-1}$, as shown by the contours in Figure 4. These capture the majority of the ribbons and loop emission.

The summed pre-flare background intensity from each box is subtracted from the summed intensity in sources above 175 DN s^{-1} $pixel^{-1}$, and the result is normalized to the maximum value of the total background-subtracted 131 Å intensity from the whole field-of-view. This results in the dotted, dashed, and dot-dashed curves in the upper panel of Figure 5. The normalized and background-subtracted *GOES* 1–8 Å emission is shown as a solid curve. Between around 17:58 UT and 18:08 UT the southern loops dominate the 131 Å intensity. The emission from the northern regions, which include ribbons and later on loops, becomes significant (~10% level) at 18:05 UT and starts to dominate the southern sources after 18:08 UT. We conclude that there is a period from about 18:08 to 18:10 during which the AIA 131 Å light curves, and by implication the *GOES* light curves, have a strong or even dominant contribution from the flare ribbons and footpoints. After around 18:10 the emission labeled "northern ribbons" in Figure 5 develops a strong contribution from the loops which start to appear in the corresponding box. In the "northern footpoints" box, however, loops do not appear until later and the bursty character of the emission that one would associate with footpoints or ribbons rather than loops is apparent for longer—up to around 18:12. We reason that this

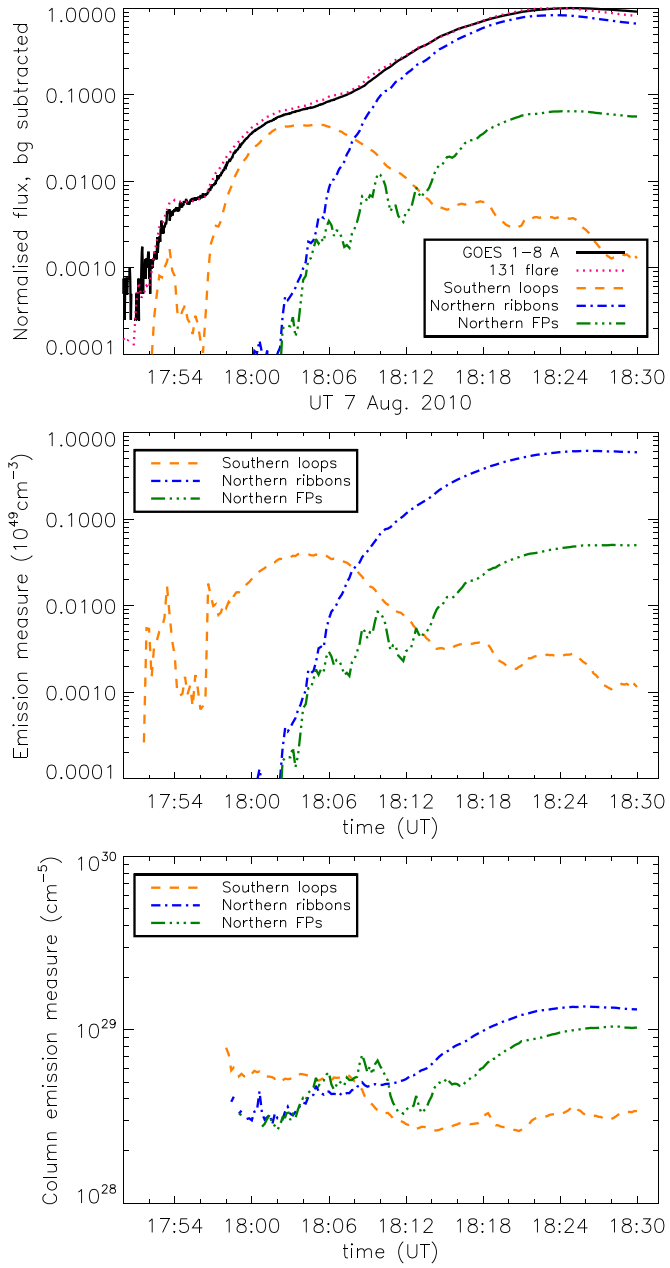

Figure 5. Upper panel: background-subtracted and normalized (to peak values) *GOES* 1–8 Å flux (black solid curve) and *SDO*/AIA 131 Å intensity of sources above 175 DN s^{-1} pixel^{-1} summed over the whole field-of-view of Figure 4 (pink dotted line), the southern loops (orange dashed line), northern ribbons (blue dot-dashed), and the subset of northern footpoints (green dash-triple-dot line). Center panel: volume emission measures inferred from the 175 DN s^{-1} pixel^{-1} thresholded sources in each of the boxes outlined in Figure 4. Lower panel: column emission measures. After 18:10 UT the integrated emission is dominated by loops.

(A color version of this figure is available in the online journal.)

bursty behavior would be visible in the northern ribbons more generally, were it not masked by the appearance of the loops.

Since the normalized AIA 131 Å emission tracks the *GOES* 1–8 Å emission very closely, we may reasonably assume that on the whole they originate from the same plasma. It should be noted, however, that the 131 Å band contains strong Fe VIII lines as well as the Fe XXI lines, so in Section 4.5 we employ a DEM analysis to further investigate the plasma temperature. Multiplying the *GOES* EM by the fractional 131 Å intensity associated with the different resolved AIA sources provides an estimate of the EM associated with each, shown in the center panel of Figure 5. So for example between 18:06:00 UT and 18:12:00 UT, the small group of northern footpoints has an EM of between $\sim 3 \times 10^{46}$ and 8×10^{46} cm^{-3}, while the northern ribbons as a whole at 18:10 UT have an EM of 7×10^{47} cm^{-3}. Dividing through by the total area (at the Sun) of the pixels in each source box above the limit of 175 DN s^{-1} pixel^{-1} we arrive at an estimate of the column EM for the hot ribbon plasma, shown in the lower panel of Figure 5. This varies the increases from 3 to 7×10^{28} cm^{-5}, between 18:00 and 18:12 UT.

4.4. Overlays of Flare Sources on *SDO*/HMI

Overlays of the 131 Å flare sources on the nearest-in-time Helioseismic and Magnetic Imager (HMI) line-of-sight magnetogram shown in Figure 6 demonstrate that the ribbons are mostly located in magnetic plage regions, but also that there are ribbon sources in weak-field regions, e.g., around $(-570'', 160'')$. These sources tend to be weaker in the EUV than their neighbors, and overlays with *RHESSI* (Figure 10) also suggest an absence of *RHESSI* sources at this location.

4.5. *SDO*/AIA Differential Emission Measure

Hannah & Kontar (2012) have developed a method of deriving the DEM from AIA observations, using regularized inversion. This permits an estimate to be made of the amount of plasma as a function of temperature at different locations in the flare, and provides estimates of both the DEM uncertainty and the effective temperature resolution. This method is applied to the three boxed regions highlighted in Figure 4, again selecting only pixels within the box which are above the 175 DN s^{-1} pixel^{-1} threshold. We have also concentrated on the time after 18:05 UT, when the ribbon emission is starting to become important. The source areas estimated from the 131 Å images are used to convert the volume DEM into a column DEM.

The DEMs are made using the six AIA EUV channels, and the accuracy of the results depends on our knowledge of the spectral lines in the channels. As shown by simultaneous spectroscopic and imaging observations with the *Hinode* EUV Imaging Spectrometer (EIS) and *SDO*/AIA, several of the observed transition region lines are omitted or poorly represented by Chianti (Del Zanna et al. 2011). In Figures 7 and 8 we show results using the AIA temperature response functions (Boerner et al. 2012) calculated at the default pressure in Chianti of 10^{15} cm^{-3} K, and also using contribution functions calculated using a greatly increased pressure of 10^{18} cm^{-3} K which may be appropriate for flaring conditions. We also include the recent normalizations implemented to provide good agreement with *SDO*/EVE; empirical corrections to the 94 Å and 131 Å channels compensate for the omissions in the Chianti database (Testa et al. 2012). With these corrections the response of *SDO*/AIA to high and low temperature flare emission is believed to be accurate to 25%.[4] These are however empirical corrections and improvements to the Chianti atomic database are required and currently being studied.

DEM analysis proceeds under assumptions of thermal and ionization equilibrium, and of optically thin radiation, and we must consider the validity of these assumptions under flaring conditions. A more detailed discussion is available in Graham et al. (2013). A slow flare evolution in the early phase

[4] http://sohowww.nascom.nasa.gov/solarsoft/sdo/aia/response/chiantifix_notes.txt

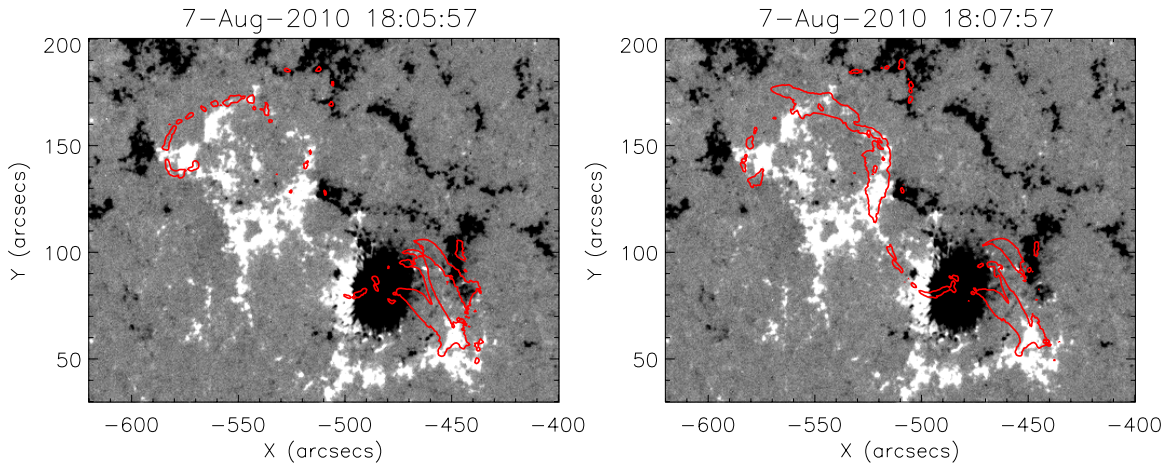

Figure 6. Overlays of the 131 Å flare sources on HMI line-of-sight magnetograms. Contours are at 200 DN s^{-1}.
(A color version of this figure is available in the online journal.)

means that, even at these high flare temperatures, equilibrium assumptions are likely to be adequate in flare footpoints. This is because the footpoint density is relatively high; we estimate $n_e \sim 10^{10}\,\mathrm{cm}^{-3}$ (see Section 6.3 and Graham et al. 2011). High density ensures that the core of the electron distribution reaches thermal equilibrium quickly, even at high temperatures, unless there is a very short heating timescale. In the case of slow heating, departure from ionization equilibrium is small for densities above $10^{10}\,\mathrm{cm}^{-3}$ (Bradshaw 2009). Low opacity in all of the main contributing lines formed at temperatures greater than 10^6 K can be verified using oscillator strengths from the Chianti database and Equation (1) from Bloomfield et al. (2002). The Fe IX line at 171.07 Å that dominates the AIA/171 channel has a large oscillator strength, and thus a larger opacity. However, even under the most pessimistic assumption (of coronal abundances) its total optical depth is less than unity for column depths under $\sim 10^{18}\,\mathrm{cm}^{-2}$, and smaller still if photospheric abundances are used. We conclude that the assumption of optically thin emission is reasonable in the footpoints of this flare, even given the rather dense plasmas we find.

The DEMs calculated for the two values of pressure are similar in shape and in magnitude, with variations everywhere less than a factor two. At $p = 10^{18}\,\mathrm{cm}^{-3}$ K, the DEM is slightly larger at $\log T \sim 6$ and slightly smaller at $\log T \sim 6.5$–7 than the corresponding value at $p = 10^{15}\,\mathrm{cm}^{-3}$ K. Each of the DEMs shown in Figure 7 has three significant bumps, at around $\log T \sim 5.9$–6, $\log T \sim 6.3$–6.4, and $\log T \sim 7.0$–7.1. At the lower temperatures it is expected that there will also be a contribution from the ambient coronal plasma in the line-of-sight between the observer and the flare sources. The largest values of high-temperature DEM are found in the southern loops, but the ribbons and footpoints also have substantial amounts of high-temperature plasma. There is some evidence that, over the 4 minutes examined, the amount of plasma at 10^6 to $10^{6.3}$ K plasma in the ribbons decreases while the amount of 10^7 K plasma stays relatively constant. However, the uncertainties on the DEM recovery make it hard to be definitive about this. There does appear to be a significant decrease in the EM at around $\log T = 6.7$ in the northern footpoints at 18:07 UT. We note this, but do not currently have an explanation. It may be a numerical instability in the reconstruction, though the error bars look very similar to the other cases. It is unlikely to be due to the loss of material from the region with the coronal mass ejection, because the DEM is generated just from the footpoint sources above some threshold intensity. Any decrease in the amount of material at $\log T = 6.7$ due to evaporation would presumably also lead to a decrease in the overlying $\log T = 7$ material, which is not seen. A pixel-by-pixel examination of the EM distribution, which we plan for a future paper, may shed light on this.

The units of the DEM are $\mathrm{cm}^{-5}\,\mathrm{K}^{-1}$, and an estimate of the EM in units of cm^{-5} at each temperature can be obtained by multiplying by that temperature, meaning that the peak at 10^7 K has the largest EM contribution, of $\sim 5 \times 10^{28}\,\mathrm{cm}^{-3}$. This is consistent with the EM values obtained from *GOES* at 10^7 K. We note also that EIS spectroscopy has been used in other events to demonstrate the presence of substantial amounts of 10 MK footpoint plasma (Graham et al. 2013).

5. *RHESSI* SPECTROSCOPY AND IMAGING

The time between 18:00:30 UT and 18:12:30 UT is split into intervals of 60 s, and *RHESSI* spectra are fitted in electron space, with an isothermal plus single power-law fit, using the OSPEX spectral fitting software. The fit assumes that the non-thermal emission originates from a cold, collisional thick target. The thermal component is parameterized by a single temperature and EM. The non-thermal electron spectrum is parameterized by the total number of electrons per second above the low-energy cutoff, E_c, and the electron spectral index δ. The fit results are shown in Figure 9. No fit parameters are shown between 18:09:30 UT and 18:10:30 UT, as this coincided with the change in the attenuator state. The spacecraft entered night at 18:12 UT.

The *RHESSI* normalized count rates, shown in the upper panel of Figure 9, are very stable for the first few minutes of the flare. At 3–6 and 6–12 keV the count rate is almost constant between 18:00:30 UT and 18:06:30 UT, followed by a smooth increase in intensity. Images at this time show that the emission is dominated by the hot southern loops, with no ribbon emission visible at the 10% level. The 12–25 keV intensity increases gradually from around 18:04 UT. Between 18:00:30 UT and 18:10:30 UT the *RHESSI* EM increases gradually from 2.5 to $5 \times 10^{47}\,\mathrm{cm}^{-3}$ (panel 2 in Figure 9). Since the AIA analysis in Section 4.3 indicates that from 18:06 UT the southern loop EM is decreasing, the increase in the *RHESSI* count rates and EM after this time, and up until

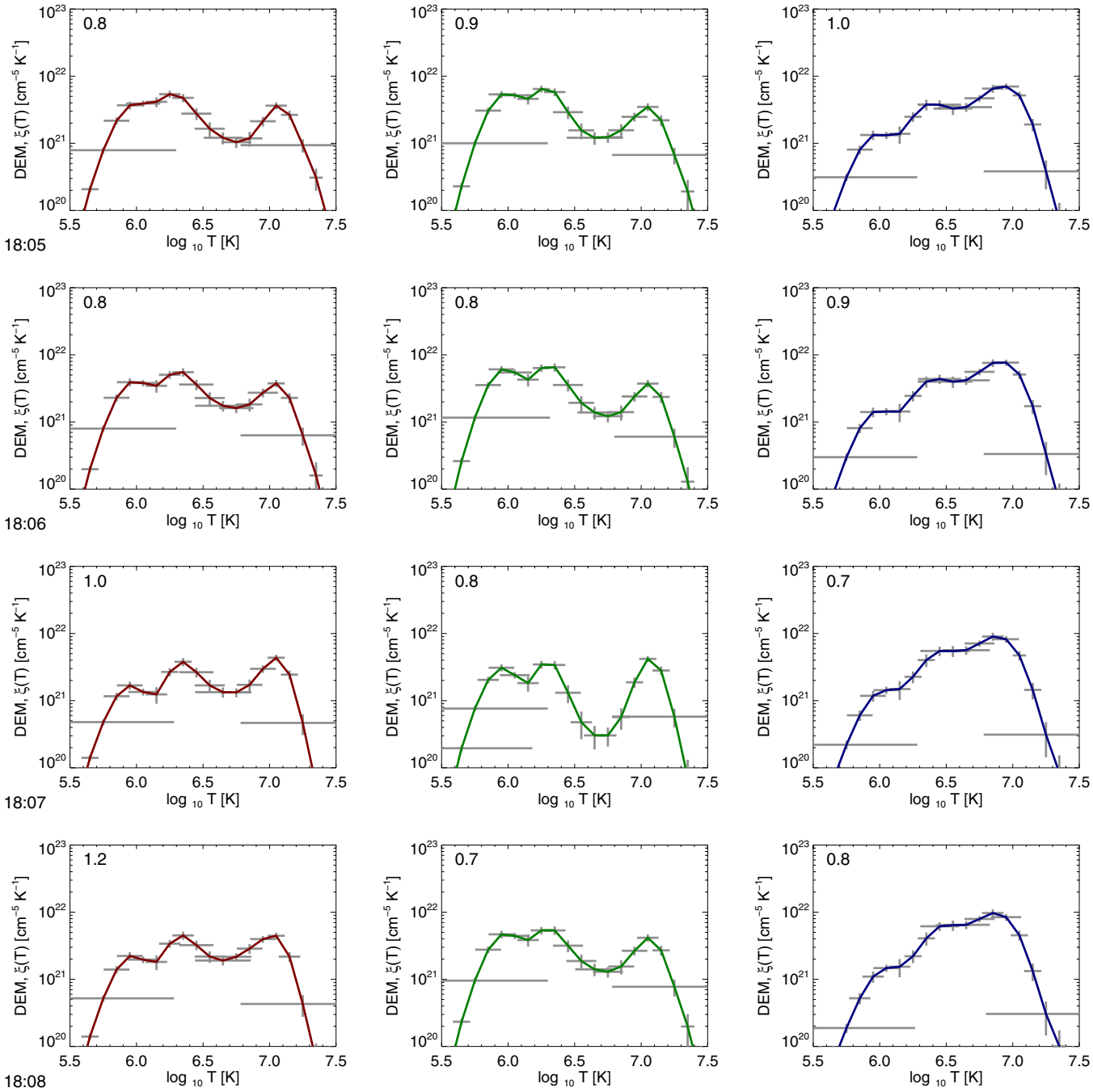

Figure 7. DEM from three different regions in the flare: left column—northern ribbons and (later) loops; center column—northern footpoints; right column—southern loops. Each row corresponds to the time indicated underneath. These have been calculated for the default Chianti pressure of 10^{15} cm^{-3} K. Note that the temperatures with very large horizontal error bars do not just indicate a bad temperature resolution but a poorly recovered DEM solution at those points (Hannah & Kontar 2012). The χ^2 between the data and the recovered DEM is indicated in the top left corner of each panel.

(A color version of this figure is available in the online journal.)

18:10 UT, is most likely attributable to the northern ribbons. The *RHESSI* EM varies from 4–7 × 10^{47} cm^{-3} between 18:06 and 18:09 UT, which is broadly consistent with the values obtained from *GOES*. The temperature (Figure 9, panel 3) decreases slightly from 11.5 MK to 10.5 MK at 18.07 UT before rising again, possibly also due to the brightening of the northern ribbons.

The spectrum, which starts off very soft, hardens abruptly between 18:06 UT and 18:10 UT as the ribbons brighten (Figure 9, panel 5). This is reflected also in the increasing electron flux during this time (panel 4) and the decrease in spectral index from 8 to 6. The fitted low-energy cutoff remains approximately constant throughout, at around 12–13 keV (panel 6).

The CLEAN algorithm with natural weighting is used to generate images using detectors 2–8, in energy bands 3–6, 6–12, and 12–25 keV. (Note, the flare occurred three months after *RHESSI*'s second anneal. Prior to this anneal, use of detector 2 had not been recommended because it was not segmenting properly, but following the anneal it recovered this capability and was included in our imaging analysis.) Integration times were 60 s, starting at 18:05:30, 18:06:30, 18:07:30, and 18:08:30. In Figure 10, *RHESSI* contours are shown overlaid on AIA 304 Å

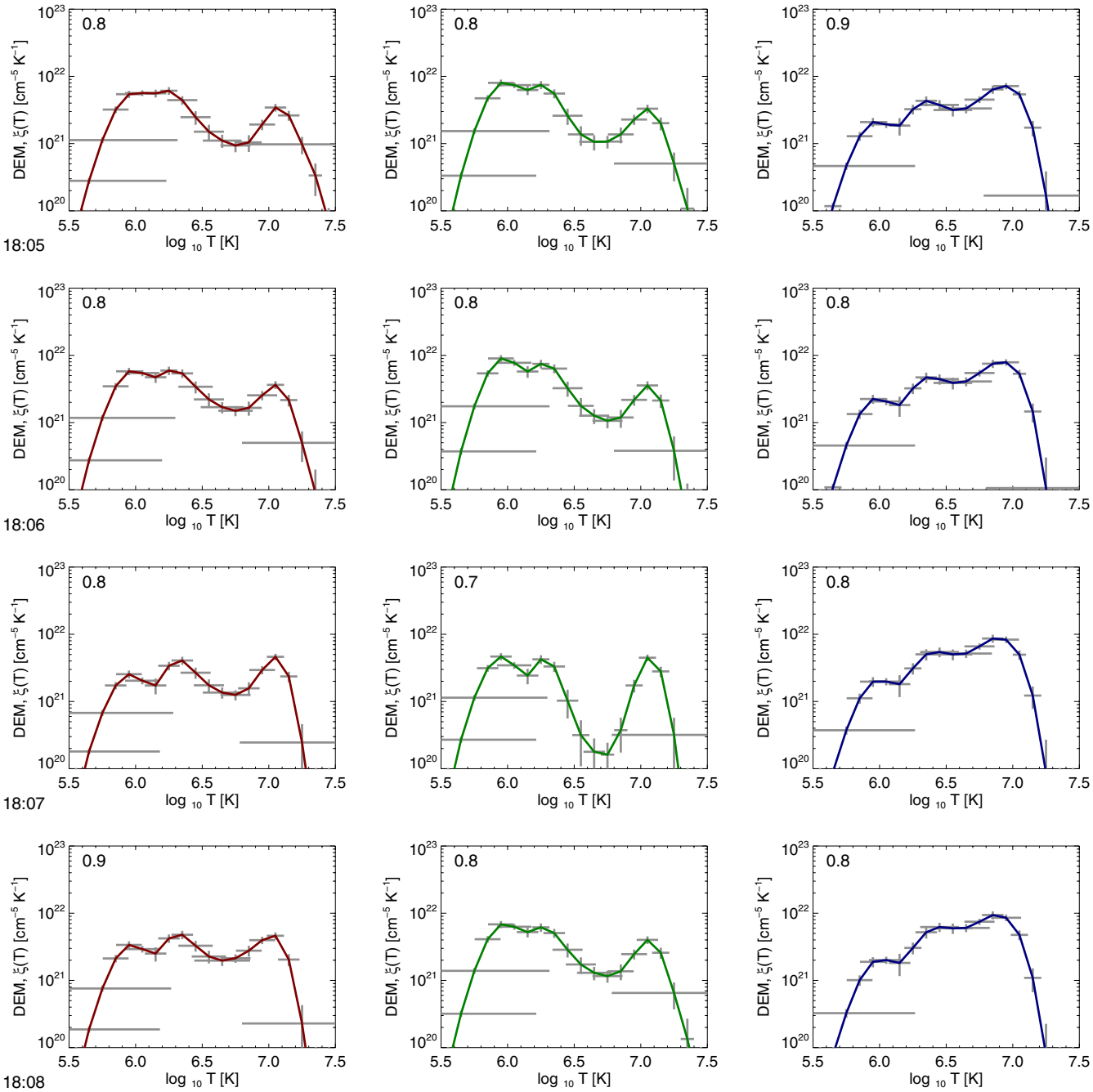

Figure 8. Same as Figure 7 but calculated for a pressure of 10^{18} cm^{-3} K.
(A color version of this figure is available in the online journal.)

and AIA 131 Å images taken at the center of the integration period. The contours show the same absolute count values in the first three image, and increase by a factor two in images 4 and 5. This makes clear the development of the absolute and relative intensities in each wavelength band. As time progresses, the ribbons become brighter relative to the southern loops at all energies, and in the two lower energy channels the emission is relatively uniform along the ribbons. At 12–25 keV the emission has a concentration around [−490″, 80], not seen at lower energies. At early times the 12–25 keV data are noisy, but a tendency for the sources to align with the ribbons is visible. There is a good alignment between the ribbons in the *RHESSI* images and the ribbons seen in the AIA 304 Å images. The corresponding 131 Å images show a fuzzy structure as well as compact footpoints at the locations of the *RHESSI* contours, suggesting the ends of hot loops may also contribute to the *RHESSI* emission. Note, Liu et al. (2012) interpret the *RHESSI* emission as originating from the filament; we disagree with this interpretation.

6. FLARE RIBBON ENERGY LOSSES AND ENERGY INPUT

6.1. Radiative Losses

Figure 11 is a composite of the power radiated in several energy loss channels. From *GOES* we have the X-ray intensity (L_x) in 1–8 Å and 0.5–4 Å channels, and the total optically thin radiative losses (L_{rad}) of the ∼10 MK plasma detected by

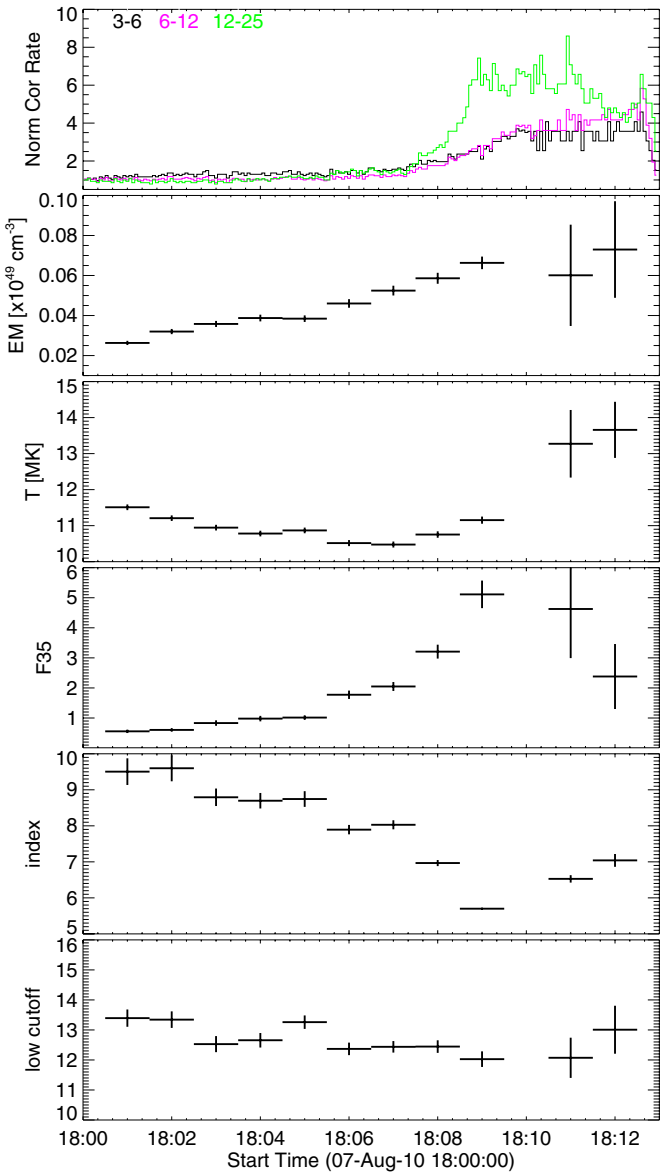

Figure 9. Evolution with time of the *RHESSI* spectral fit parameters. From the top, the panels show the normalized corrected *RHESSI* count rates in 3–6, 6–12, and 12–25 keV, the emission measure of the isothermal plasma component, the temperature of this component, the total non-thermal electron number flux, F_{35} above low-energy cutoff E_c in units of 10^{35} electrons s^{-1}, the electron spectral index δ, and the electron low-energy cutoff.

(A color version of this figure is available in the online journal.)

GOES. This is provided by the SolarSoft *GOES* software, and calculation is based on the Chianti (Version 5) spectroscopic database (Landi et al. 2006). Coronal abundances are assumed. The flare excess power in the He II 304 Å line measured by EVE is also shown, as is the power in the *SDO*/AIA 1600 Å and 1700 Å channels, calculated using the known telescope response functions in those channels.

In the first few minutes of the flare, until around 18:12 UT, the 1700 Å passband dominates the flare radiative output. The 1700 Å passband is designed to measure continuum, and has a passband of around 200 Å. Full spectrum data are not available, and the event was not detectable in AIA/HMI data, presumably being too weak. So a total radiative power budget is hard to assemble, but it is reasonable to assume that the full UV-to-optical continuum will contain perhaps 10 times the excess power in the 1700 Å passband. Kretzschmar (2011) carried out a superposed epoch analysis of flares of different classes, finding that for flares in class C4 to M2.8 the total irradiance is 250–500 times the *GOES* 1–8 Å luminosity. This would correspond to 3.75–7.5 $\times$ 10^{26} erg s^{-1} at 18:06 UT and 5–10 $\times$ 10^{26} erg s^{-1} at 18:08 UT. The multiplying factor of 250–500 represents average values over the duration of the flare; however, the longer wavelength emissions (i.e., optical to UV) which constitute the bulk of the radiated power, occur preferentially during the earlier parts of a flare. An estimate of the ratio of the irradiance enhancement to the *GOES* 1–8 Å luminosity enhancement during a flare's impulsive phase (as indicated by the maximum of the *GOES* derivative) was made in a flare reported by Woods et al. (2004). Measurements of the X17 flare SOL2003-10-28:T11:10 show an increase in the total solar irradiance at the peak of the *GOES* derivative in SOL2003-10-28:T11:10 of 268 ppm, or 360 mW m^{-2}, while the *GOES* flux at this time is around 1 mW m^{-2}. This gives a ratio of total power to *GOES* 1–8 Å power during the impulsive phase of around 360, in the middle of the range found by Kretzschmar (2011).

6.2. Energy Input from RHESSI

The *RHESSI* data provide the means to estimate the energy input to the chromosphere, under the collisional thick target assumption that the HXRs are produced by collisional bremsstrahlung during the passage of non-thermal electrons through a dense target, in which the electrons are stopped completely by Coulomb collisions. The power delivered by non-thermal electrons above cutoff energy E_c (in keV) is estimated from the electron distribution parameters shown in Figure 9, using

$$P(E > E_c) = \frac{\delta - 1}{\delta - 2} \frac{10^{35} F_{35}}{E_c} \text{ erg s}^{-1}, \quad (1)$$

where F_{35} is the total number of electrons per second above the low-energy cutoff E_c, in units of 10^{35} electrons per second and δ is the electron spectral index. The total power in electrons is shown by the triangle symbols in Figure 11. There is sufficient energy to account for the radiated components at EUV and SXR, but as mentioned previously the energetically dominant UV-optical range is not sampled. From the arguments in Section 6.1 we might expect the total power radiated to be ~360 times the *GOES* 1–8 Å luminosity, or ~10 times the 1700 Å power. This could readily be provided by a beam with the parameters inferred. There will also be conductive losses and work done to drive evaporation. We will return to the former in Section 6.3.

The *RHESSI* data also allow us to evaluate the non-thermal EM, defined as $\text{EM}_{\text{nt}} = n_{\text{nt}} n_i V$, where n_{nt} is the number density of non-thermal electrons in the source producing the HXR emission, n_i the ambient ion density in that source, and V the source volume. Knowing the thermal EM, $\text{EM} = n_e n_i V$ it is thus possible to determine the ratio of non-thermal to thermal electrons in the source. EM_{nt} is determined from the fit parameters of the photon energy (ϵ) spectrum $I(\epsilon) = A\epsilon^{-\gamma}$, e.g., Lin (1974):

$$\text{EM}_{\text{nt}} = 3.85 \times 10^{41} A \gamma (\gamma - 1)^2 B\left(\gamma - \frac{1}{2}, \frac{3}{2}\right) \int_{E_c}^{\infty} E^{-\gamma + 1/2} dE, \quad (2)$$

giving EM_{nt} corresponding to non-thermal electron energy $E \geqslant E_c$. Here, γ is the photon spectral index ($= \delta - 1$ in

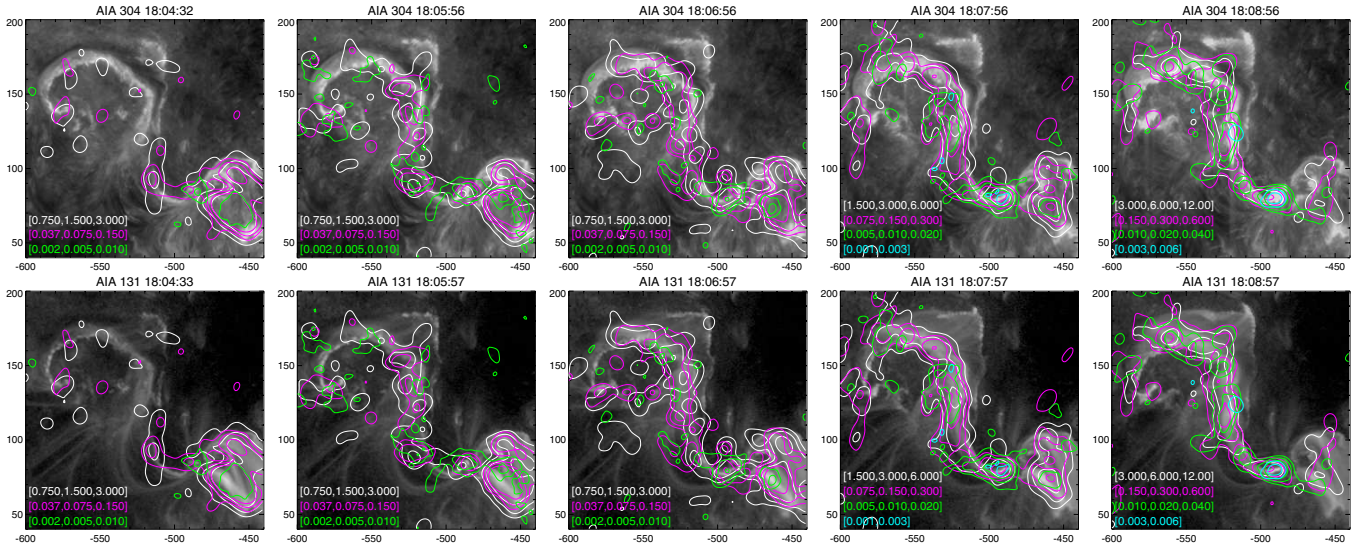

Figure 10. *RHESSI* images made using the CLEAN algorithm and data from detectors 2–8. Contours plotted are absolute values, in counts s^{-1} detector^{-1} keV^{-1} as shown in the lower left of each panel. In the first three columns, contours shown all have the same absolute values between images. Contours are 3–6 keV (white), 6–12 keV (pink), 12–25 keV (green), and in the rightmost two columns also 25–50 keV (cyan). Axes are arcseconds from disk center.

(A color version of this figure is available in the online journal.)

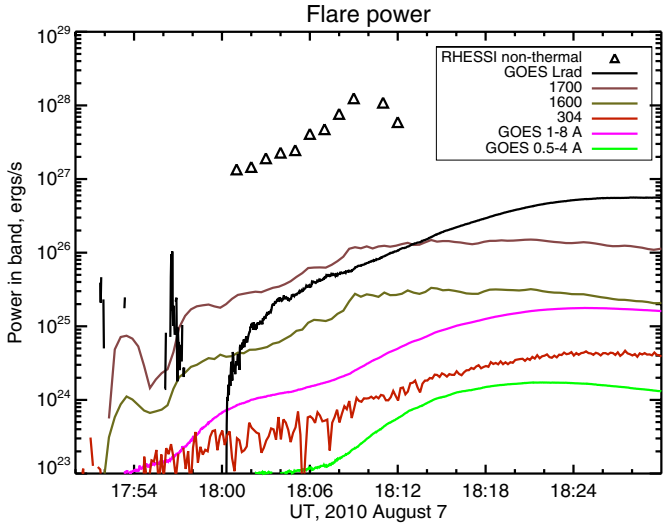

Figure 11. Power input and radiated from entire flare. Symbols show the *RHESSI* energy input rates, assuming a collisional thick-target electron beam. Magenta and green are the *GOES* 1–8 Å and 0.5–4 Å luminosities, and the black line is the calculated optically thin radiation from the plasma detected by *GOES*. The red line is the excess EVE 304 Å power, and the pink-brown and sage lines are the excess *SDO*/AIA 1700 Å and 1600 Å powers.

(A color version of this figure is available in the online journal.)

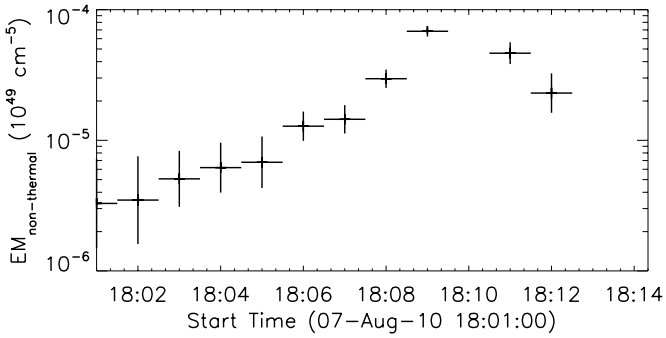

Figure 12. Non-thermal emission measure for the event, calculated from the flare-integrated *RHESSI* spectrum. Error bars are calculated from errors on the fit to the photon spectral index.

the thick target chromosphere), and B is the beta function. This gives the instantaneous number of non-thermal electrons in the radiating plasma. The relationship assumes that the HXR emission is due to collisional bremsstrahlung, but does not require the assumption of a thick target. Again using the fit parameters shown in Figure 9, we arrive at the values for the non-thermal EMs shown in Figure 12. These values are 10^3 to 10^4 times lower than the typical thermal EMs $n_e n_i V$ obtained from *RHESSI* (Figure 9). In other words, averaging over all the plasma observed by *RHESSI*, one electron in 10^3–10^4 has energy higher than the low-energy cutoff obtained from spectral fitting. The fraction of non-thermal electrons increases with time to a peak at some time between 18:09 and 18:11 UT.

6.3. Power Budget of the ~10 MK Ribbon Plasma

Here we examine in further detail the energy gains and losses from the 10 MK plasma in the ribbons identified with *GOES*, *SDO*/AIA, and *RHESSI*. The total collisional power input $P_{\rm coll}$ erg s^{-1} to the heated part of the atmosphere can only be inferred from the collisional thick-target model by integrating the energy loss ΔE per particle transiting over the electron distribution:

$$P_{\rm coll}(N) = \int_{E_c}^{\infty} F_o E_o^{-\delta} \Delta E(E_o, N) dE_o, \qquad (3)$$

where $N = \int n_e dl$ is the column depth of the heated plasma, and $\Delta E = E_o - E(N)$, with $E(N)$ being the energy of an electron of initial energy E_o after it has traversed N. The subscript o refers to the properties at injection into the chromosphere, i.e., the collisional thick target properties determined from spectral fitting. From Emslie (1978), $E(N)^2 = E_o^2 - 3\Lambda K N$, where Λ is the Coulomb logarithm and $K = 2\pi e^4$, e being the charge of the electron. This approximation assumes that electrons enter as a unidirectional beam along the magnetic field direction (assumed vertical) and we take $\Lambda = 20$ which is appropriate for the fully ionized plasma of the upper chromosphere.

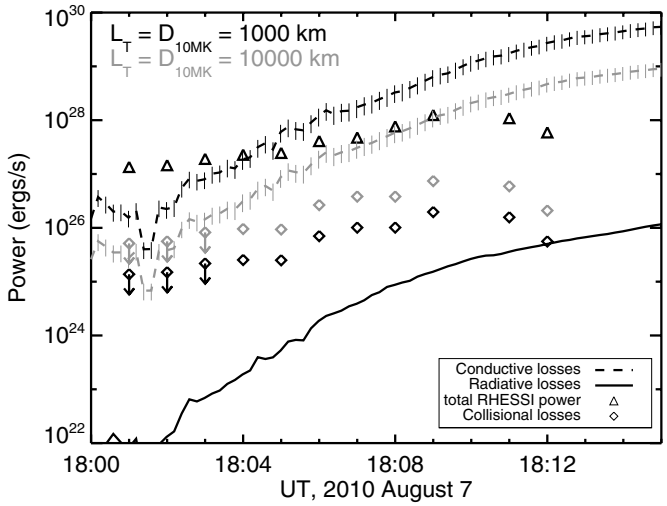

Figure 13. Total non-thermal power delivered to the flare (triangles) and the collisional power input to the 10 MK plasma only (diamonds) compared to the radiative and collisional losses from the 10 MK plasma, assuming values of 1000 km (black) and 10,000 km (gray) for the thickness of the 10 MK plasma/temperature scale length. Error bars on $L_{\rm cond}$ are shown for an uncertainty of 1 MK in the temperature of the hot plasma.

Substituting for ΔE in Equation (3) and performing the integral gives

$$P_{\rm coll}(N) = F_{\rm tot} E_c \frac{\delta - 1}{\delta - 2}\left[1 - \left(\frac{\delta}{2} - 1\right) x_c^{1-\delta/2} B \times \left(x_c; \frac{\delta}{2} - 1, \frac{3}{2}\right)\right], \quad (4)$$

where

$$x_c = \frac{3KN}{E_c^2} \quad (5)$$

and B is now the incomplete beta function. We also use

$$F_{\rm tot} = \int_{E_c}^{\infty} F_o E_o^{-\delta} dE_o, \quad (6)$$

where $F_{\rm tot}$ is the total number of electrons per second injected above $E = E_c$.

N can be estimated from the footpoint (column) EM as $N \sim n_e L \sim ({\rm EM}L)^{1/2}$, for a uniform source of thickness L. The AIA ribbon sources in all channels co-align to better than one or two pixels, so that if the 10 MK plasma sits above the AIA sources at 304 Å then the maximum thickness of the 10 MK plasma should be ~1000 km (comparable also to the thickness of the chromosphere). Using the observed EM of $\sim 5 \times 10^{28}$ cm^{-5} gives a density $n_e \sim 2 \times 10^{10}$ cm^{-3}, with column depth N of $\sim 2 \times 10^{18}$ cm^{-2}. Assuming a smaller source thickness of ~100 km results in $n_e \sim 7 \times 10^{10}$ cm^{-3} and column depth $\sim 7 \times 10^{17}$ cm^{-2}.

The calculated values of $P_{\rm coll}$ for a source thickness L = 1000 km are shown by the diamonds in Figure 13. In this figure we have also applied a scaling to account for the fact that not all of the HXR emission comes from the ribbons. We have estimated the fraction of the non-thermal electron power delivered to the northern ribbons by multiplying the total power by the ratio of 12–25 keV flux summed over the northern box (shown in Figure 4) to the total 12–25 keV flux in the *RHESSI* image.

Decreasing the thickness of the 10 MK source will decrease the collisional power input to the source. For completeness we also show losses for the case where the source thickness is increased to 10,000 km.

The hot plasma emits optically thin radiation at rate $L_{\rm rad}$ erg s^{-1}, as discussed in Section 6.1, and we obtain the ribbon contribution by again scaling the total $L_{\rm rad}$ by the fractional 131 Å intensity from the northern ribbon sources (Figure 5). The hot plasma must also lose energy by conduction to cooler, lower layers of the atmosphere at rate $L_{\rm cond}$ erg s^{-1}. The conductive losses are estimated following the approach of Battaglia et al. (2009) for flux-limited conduction. Flux-limited conduction applies because the chromospheric temperature scale length L_T is small, referring again to the small separation between the 10 MK plasma imaged by the AIA 131 Å and 304 Å channels. So the electron collisional mean-free path $l_{\rm mfp} = 5.21 \times 10^3 T^2/n_e$ is significant compared to the temperature scale length. Non-local effects become important and classical Spitzer conductivity will not apply. A modification to the normal heat-flux equation is necessary, with the conductive flux $F_{\rm cond}$ (erg cm^{-2} s^{-1}) given by

$$F_{\rm cond} = \varrho(x) F_{\rm class} = \varrho(x) \kappa_o T^{5/2} \frac{dT}{dz}, \quad (7)$$

where the classical Spitzer conductivity constant κ_o is reduced by a factor ϱ, which is a function of $x = \log(l_{\rm mfp}/L_T)$, the logarithm of the ratio of the electron mean-free path to the temperature scale length. Battaglia et al. (2009) fitted a functional form to the values of ϱ published by Campbell (1984) obtaining

$$\varrho(x) = 1.01 e^{-0.05(x+6.63)^2}. \quad (8)$$

Approximating dT/dz by T/L_T, and taking $T = 10$ MK and $L_T = 10^3$ km we can calculate the conductive flux, using also the value of n_e determined from the EM. With these values, the modification due to non-local conduction reduces $F_{\rm cond}$ by a factor 10 over the interval 18:00 UT to 18:12 UT, compared to the classical value. $L_{\rm cond}$ is then obtained by multiplying $F_{\rm cond}$ by the total area of the hot northern ribbon sources observed in the 131 Å channel. The results for radiative and conductive losses, and energy input, are shown in Figure 13.

These calculations demonstrate firstly that conductive losses dominate radiative losses from the 10 MK ribbon plasma, and secondly that collisional energy losses in the 10 MK ribbon plasma, inferred from the collisional thick target calculation, are inadequate to supply the calculated conductive losses, by a factor of about 100 in the case of a source thickness of 1000 km. However, the low-energy cut-off value E_c on which the thick-target calculation depends is notoriously difficult to fit. If the value of E_c is reduced to a fraction f of the fitted value then the arrival rate of non-thermal electrons is increased by $f^{(1-\delta)}$, and the power delivered by $f^{(2-\delta)}$. A value of f = 0.4–0.5 (i.e., E_c around 4–6 keV) would thus provide adequate input power to balance the losses (the total beam power would also be increased). However, E_c is then close to the typical thermal energy of electrons in the 10 MK plasma and it is not clear that "thermal" and "non-thermal" populations can be separated. Such a low cut-off energy also means that the cold collisional thick target approximation is not applicable to the whole distribution (see Section 7).

We note also that if the calculation is repeated for the case of electrons injected at some non-zero pitch angle to the magnetic field, the effect is to introduce a factor μ (equal to the pitch-angle cosine) on the denominator of Equation (5). The corresponding increase in x_c results in an increase in $P_{\rm coll}$. For example, for $\mu = 0.3$, values of $P_{\rm coll}$ typically increase by a factor two.

7. DISCUSSION

This event provides a good opportunity to study the earliest phases of a large flare, in particular investigating the thermal and non-thermal properties of the flare ribbons. By demonstrating that the *GOES* and *SDO*/AIA 131 Å light curves track each other closely, and using AIA image data, we identify an interval between ~18:05:00 UT and 18:10:00 UT during which a significant or even dominant fraction of the *GOES* emission comes from the flare ribbons, originating in or just above the chromosphere. We infer from *GOES* and AIA imaging that the ribbons contain ~10 MK plasma with a column EM of typically a few times 10^{28} cm^{-5}. This is backed up by AIA DEM analysis carried out on the flare ribbons, and also by *RHESSI* imaging and spectroscopy, which shows significant or dominant contributions to the thermal emission from the ribbons at this time. The conclusion is that the lower atmosphere is very strongly heated during the early phase of the flare. This is consistent with previous (but mostly overlooked) observations of so-called impulsive SXR footpoints (e.g., McTiernan et al. 1993; Hudson et al. 1994; Mrozek & Tomczak 2004).

In common with previous studies of the pre-flare we find that the initial brightening, in the southern loops, is located in a different place from the main flare ribbons. The southern loops dominate in *RHESSI* until ~18:06 UT and cause a distinct bump in the *GOES* and *SDO*/AIA 131 Å intensity. After 18:05 UT the ribbon emission starts to become important, and over the next few minutes there follows a strong increase in the inferred electron flux, and decrease in the electron spectral index. The typical column EM in the ribbons increases by about a factor of two between 18:00 UT and 18:10 UT, which could correspond to the heating of deeper, denser layers of the chromosphere as the energy deposition rate increases. The increase in the total EM from the ribbons is caused mostly by an increase in the volume of hot plasma as the ribbon area increases.

The HXR spectrum from the entire flare region can be fitted by a thermal source with temperature approximately 10 MK, and a steep non-thermal spectrum with a low energy cutoff varying between 12 and 13 keV. Using standard thick-target expressions to interpret the non-thermal HXR spectrum and—by assuming the relationship between 1–8 Å *GOES* X-ray luminosity and the flare total solar irradiance found by Kretzschmar (2011)—it appears that the energy present in the non-thermal electrons can account for the totality of the radiated emission to be expected from this event.

In addition, the energy budget of the 10 MK plasma of the northern ribbons is studied, comparing the collisional energy input to this plasma with radiative and conductive energy loss rates. Here it is found that to support the calculated conductive losses, the low-energy cutoff of the electron spectrum should be around 4 to 6 keV. Enthalpy flux from this plasma, i.e., chromospheric evaporation into overlying loops, is not considered but would place additional demands on the energetics.

A low-energy cutoff of only a few times the typical thermal energy of $kT \sim 1$ keV has two consequences. First, the injected electrons near the cutoff would be in the warm-target regime $kT \lesssim E \lesssim 5kT$ meaning that they experience both energy loss and energy gain in their interactions with the surroundings. Second, the existence of two separate distributions (i.e., thermal and non-thermal) becomes questionable. Emslie (2003) assesses the flare energetics under the collisional thick-target assumptions, including the effect of the warm target, in the case where instead of a low-energy cutoff the power-law part of the spectrum continues smoothly into the thermal component. In such a scenario, and for electron spectral indices in the range $\delta = 6$–9, as we find in this flare, the total injected electron power would be 5×10^4 to 5×10^7 times the collisional thick-target power determined for electrons above E_c (shown in Figure 11) or $\sim 10^{34}$ erg s^{-1}, which is quite unreasonable.

We may consider an alternative scenario, which does not involve the injection of non-thermal electrons from the corona, but supposes their acceleration in situ in chromospheric plasma that has been heated by some other means. Together, the thermal and the non-thermal EMs determined for the event indicate that approximately one electron in 10^4 at an energy greater than the fitted low-energy cutoff of ~10 keV is required, if we assume that the thermal and non-thermal EMs are generated in the same plasma. For our estimated n_e, this would correspond to a non-thermal electron number density of 2×10^6 cm^{-3}. At the peak of the HXRs, the requirement is one electron in 10^3. In principle, energy could be deposited in the plasma by some means other than electron collisions, for example by waves or turbulence, resulting first in electron heating and then in the acceleration of a high energy tail (e.g., Liu & Fletcher 2009). We do not specify here what that heating/acceleration mechanism might be, but possibilities do exist—for example electron Landau resonance in Alfvénic turbulence, as explored by Bian et al. (2010). The electron spectrum will then be determined by both the acceleration rate as a function of electron energy and the collisional loss rate. It is worth pointing out that if electron energy losses are dominated by collisions, the instantaneous *power* in the non-thermal electron spectrum required to explain the non-thermal bremsstrahlung emission is the same as in the standard collisional thick-target model, however the *number* of non-thermal electrons required to produce the emission can be significantly reduced, basically because any local acceleration increases the effective radiating lifetime of an individual electron compared to the case where its energy evolution is determined by collisional losses alone. More discussion of this can be found in Brown et al. (2009).

The pre-flare chromosphere is so cool, dense, and collisional that any energy input will initially result only in heating. The electron–electron collision timescale for electrons in the thermal core of a Maxwellian distribution of temperature T and density n_e is (e.g., Somov 2006)

$$\tau_{ee} = \frac{m_e^2 (3kT_e/m_e)^{3/2}}{8\pi e^4 n_e \Lambda} \frac{1}{0.714}, \tag{9}$$

where m_e is the electron mass and e the elementary charge. So as the plasma heats up, the collision timescale increases as $T^{3/2}$. For electrons of energy E in the tail of the Maxwellian, the electron–electron collision timescale increases to $\tau_{\rm tail} = \chi^{3/2}\tau_{ee}$, where $\chi = E/kT$. So eventually some electrons out in the tail will become collisionless, in the sense that for these electrons the energy-input timescale becomes shorter than $\tau_{\rm tail}$. These electrons may then be accelerated.

The fraction of electrons in the tail of a Maxwellian, above some energy $E = \chi kT$, is

$$f_\chi = \left(\frac{4\pi}{\chi}\right)^{1/2} e^{-\chi} \tag{10}$$

for $\chi \gg 1$. Observations require an accelerated fraction $f_\chi = 10^{-3}$, meaning that $\chi = 7.1$. If $f_\chi = 10^{-4}$ then $\chi = 9.3$. For a Maxwellian core temperature of 10 MK and a density of 2×10^{10} cm^{-3} we find $\tau_{ee} \sim 0.02$ s, therefore to accelerate

the electrons in the tail would require an energization process operating in the chromosphere with energy input timescale to these electrons of $\lesssim \tau_{\rm tail} = 0.02 \times \chi^{3/2} \sim 0.02 \times 9^{3/2} \sim 0.5$ s.

We remark that any collisional losses undergone by the locally accelerated electrons cannot contribute substantially to the heating. The instantaneous energy density in the 10 MK plasma is $n_e kT \sim 28\,{\rm erg\,cm^{-3}}$ for $n_e \sim 2 \times 10^{10}\,{\rm cm^{-3}}$, whereas the instantaneous energy density in the non-thermal electrons is $\sim 10^{-3} n_e E$ where E, the energy of the electrons, is typically 10 keV, giving an energy density in the non-thermals of $\sim 0.3\,{\rm erg\,cm^{-3}}$.

A variant on this scenario could involve the injection of a small number of non-thermal electrons from the corona, which are locally re-accelerated in chromospheric turbulence or current sheets (Brown et al. 2009). But the requirement to identify a source of heating for the 10 MK ribbon plasma, other than collisional losses, remains. As mentioned before, both the EUV emission and the *RHESSI* X-rays in the main ribbons appear to be weaker in regions of weaker magnetic field. We have not examined this in any detail but the HMI information on magnetic field, coupled with the ability to examine the AIA DEM on a pixel-by-pixel basis (Hannah & Kontar 2013) will enable us to investigate possible correlations in detail.

Flares like this in *SDO*/AIA with a long, well-observed onset are relatively rare, since usually image saturation quickly becomes a problem. However, numerous events are expected to be unsaturated at least for the first few seconds of the impulsive phase, and it will be interesting to see whether 10 MK ribbon plasma is confirmed in other *SDO* events.

We are grateful to an anonymous referee for insightful comments that led to improvements in our analysis and presentation. L.F. and H.S.H. thank the Max Planck Institute for Solar System Research for travel support and hospitality. *SDO* data come courtesy of NASA/*SDO* and the AIA, EVE, and HMI science teams, and we are grateful to NASA for its open data policy which enables work such as this. This research was supported by STFC rolling grant ST/I001808/1, by Leverhulme grant F00-179A, and by EC-funded FP7 project HESPE (FP7-2010-SPACE-1-263086).

REFERENCES

Battaglia, M., Fletcher, L., & Benz, A. O. 2009, A&A, 498, 891
Bian, N. H., Kontar, E. P., & Brown, J. C. 2010, A&A, 519, A114
Bloomfield, D. S., Mathioudakis, M., Christian, D. J., Keenan, F. P., & Linsky, J. L. 2002, A&A, 390, 219
Boerner, P., Edwards, C., Lemen, J., et al. 2012, SoPh, 275, 41
Bradshaw, S. J. 2009, A&A, 502, 409
Brosius, J. W., & Holman, G. D. 2012, A&A, 540, A24
Brown, J. C., Turkmani, R., Kontar, E. P., MacKinnon, A. L., & Vlahos, L. 2009, A&A, 508, 993
Campbell, P. M. 1984, PhRvA, 30, 365
Chifor, C., Mason, H. E., Tripathi, D., Isobe, H., & Asai, A. 2006, A&A, 458, 965
Chifor, C., Tripathi, D., Mason, H. E., & Dennis, B. R. 2007, A&A, 472, 967
Crotser, D. A., Woods, T. N., Eparvier, F. G., Triplett, M. A., & Woodraska, D. L. 2007, Proc. SPIE, 6689, 18
Del Zanna, G., O'Dwyer, B., & Mason, H. E. 2011, A&A, 535, A46
Dere, K. P., & Cook, J. W. 1979, ApJ, 229, 772
Emslie, A. G. 1978, ApJ, 224, 241
Emslie, A. G. 2003, ApJL, 595, L119
Fárník, F., Hudson, H., & Watanabe, T. 1996, SoPh, 165, 169
Fárník, F., & Savy, S. K. 1998, SoPh, 183, 339
Feldman, U., Laming, J. M., Doschek, G. A., Warren, H. P., & Golub, L. 1999, ApJL, 511, L61
Graham, D. R., Fletcher, L., & Hannah, I. G. 2011, A&A, 532, A27
Graham, D. R., Hannah, I. G., Fletcher, L., & Milligan, R. O. 2013, ApJ, 767, 83
Hannah, I. G., & Kontar, E. P. 2012, A&A, 539, A146
Hannah, I. G., & Kontar, E. P. 2013, A&A, 553, 10
Hock, R. A., Chamberlin, P. C., Woods, T. N., et al. 2012, SoPh, 275, 145
Hudson, H. S., Strong, K. T., Dennis, B. R., et al. 1994, ApJL, 422, L25
Kretzschmar, M. 2011, A&A, 530, A84
Landi, E., Del Zanna, G., Young, P. R., et al. 2006, ApJS, 162, 261
Lemen, J. R., Title, A. M., Akin, D. J., et al. 2012, SoPh, 275, 17
Lin, R. P. 1974, SSRv, 16, 189
Lin, R. P., Dennis, B. R., Hurford, G. J., et al. 2002, SoPh, 210, 3
Liu, R., Kliem, B., Török, T., et al. 2012, ApJ, 756, 59
Liu, S., & Fletcher, L. 2009, ApJL, 701, L34
McTiernan, J. M., Kane, S. R., Loran, J. M., et al. 1993, ApJL, 416, L91
Milligan, R. O., Chamberlin, P. C., Hudson, H. S., et al. 2012, ApJL, 748, L14
Mrozek, T., & Tomczak, M. 2004, A&A, 415, 377
O'Dwyer, B., Del Zanna, G., Mason, H. E., Weber, M. A., & Tripathi, D. 2010, A&A, 521, A21
Somov, B. V. 2006, Plasma Astrophysics, Part I: Fundamentals and Practice (New York: Springer)
Srivastava, A. K., & Murawski, K. 2012, ApJ, 744, 173
Testa, P., Drake, J. J., & Landi, E. 2012, ApJ, 745, 111
Tripathi, D., Gibson, S. E., Qiu, J., et al. 2009, A&A, 498, 295
Vemareddy, P., Maurya, R. A., & Ambastha, A. 2012, SoPh, 277, 337
Warren, H. P., & Reeves, K. K. 2001, ApJL, 554, L103
Warren, H. P., & Warshall, A. D. 2001, ApJL, 560, L87
Woods, T. N., Eparvier, F. G., Fontenla, J., et al. 2004, GeoRL, 31, 10802
Woods, T. N., Eparvier, F. G., Hock, R., et al. 2012, SoPh, 275, 115